

Title

Multiple optimal phenotypes overcome redox and glycolytic intermediate metabolite imbalances in *Escherichia coli* *pgi* knockout evolutions

Authors

Douglas McCloskey^{1,2}, Sibe Xu¹, Troy E. Sandberg¹, Elizabeth Brunk¹, Ying Hefner¹, Richard Szubin¹, Adam M. Feist^{1,2}, and Bernhard O. Palsson^{1,2,*}

Affiliations

¹Department of Bioengineering, University of California - San Diego, La Jolla, CA 92093, USA.

²Novo Nordisk Foundation Center for Biosustainability, Technical University of Denmark, 2800 Lyngby, Denmark.

*Corresponding author, Department of Bioengineering, University of California, San Diego, 9500 Gilman Drive, La Jolla, CA 92093-0412, USA.

Tel.: [858-534-5668]; Fax: [858-822-3120]; E-mail: palsson@ucsd.edu

Subject terms

adaptive laboratory evolution, *pgi* gene knockout, mutation analysis, multi-omics analysis, systems biology, *E. coli*

Abstract

A mechanistic understanding of how new phenotypes develop to overcome the loss of a gene product provides valuable insight on both the metabolic and regulatory functions of the lost gene. The *pgi* gene, whose product catalyzes the second step in glycolysis, was deleted in a growth optimized *Escherichia coli* K-12 MG1655 strain. The initial knock-out (KO) strain exhibited an 80% drop in growth rate, that was largely recovered in eight replicate, but phenotypically distinct, cultures after undergoing adaptive laboratory evolution (ALE). Multi-omic data sets showed that the loss of *pgi* substantially shifted pathway usage leading to a redox and sugar phosphate stress response. These stress responses were overcome by unique combinations of innovative mutations selected for by ALE. Thus, the coordinated mechanisms from genome to metabolome that lead to multiple optimal phenotypes after loss of a major gene product were revealed.

Importance

A mechanistic understanding of how new phenotypes develop to overcome the loss of a gene product provides valuable insight on both the metabolic and regulatory functions of the lost gene. The *pgi* gene, whose product catalyzes the second step in glycolysis, was deleted in a growth optimized *Escherichia coli* K-12 MG1655 strain. Eight independent adaptive laboratory evolution (ALE) experiments resulted in eight phenotypically distinct endpoints that were able to overcome the gene loss. Utilizing multi-omics analysis, the coordinated mechanisms from genome to metabolome that lead to multiple optimal phenotypes after loss of a major gene product were revealed.

45 Introduction

46 The flux split between upper glycolysis and the oxidative pentose phosphate pathway (oxPPP)
47 at the glucose 6-phosphate (G6P) node is a major determinant of the flux state of a cell's core
48 metabolic function. This is particularly true when a cell is exposed to glucose, which is
49 commonly used in many laboratory media formulations and is found in many environmental
50 conditions in nature. Loss of Phosphoglucose Isomerase (PGI), encoded by *pgi*, induces
51 detrimental physiological consequences (1–5). Removal of *pgi* generates an imbalance in
52 glycolytic intermediates from the loss of upper glycolytic flux that leads to a loss of fitness, and
53 induces a sugar phosphate stress response. The sugar phosphate stress response involves the
54 actions of both small RNAs (sRNAs) and transcription factors (TFs) that induce transcription
55 level changes aimed at alleviating the imbalance (6–8). Removal of *pgi* also generates an
56 overabundance of NADPH and redox imbalance by redirecting glycolytic flux into the oxPPP.
57 NADPH provides reducing equivalents for biosynthesis. In addition, NADPH plays an important
58 role in reactive oxygen species (ROS) detoxification by regenerating reduced glutathione (gthrd)
59 (9). Increased availability of NADPH in *pgi*- backgrounds has proven useful in various
60 biotechnology applications in order to increase cofactor and heterologous pathway production
61 (1, 2, 10).

62

63 Adaptive laboratory evolution (ALE) of *pgi* mutants have been carried out to better understand
64 the physiological changes required to overcome genetic perturbation (3, 4). ALE is an
65 experimental method that introduces a selection pressure (e.g., growth rate selection) in a
66 controlled environmental setting (11–13). Using ALE, organisms can be perturbed from their
67 evolutionary optimized homeostatic states, and their re-adjustments can be studied during the
68 course of adaptation to reveal novel and non intuitive component functions and interactions
69 (14). Previous ALEs of *pgi* mutants have demonstrated a re-wiring of central metabolic fluxes

70 (4) and diversity in endpoint physiological phenotypes (3). The diversity in endpoint
71 physiological phenotypes is directly attributed to the existence of alternate optimal metabolic
72 and regulatory network states that can achieve the same physiological function (3). However,
73 the mechanisms and coordination of the regulatory and metabolic network required to produce
74 physiologically distinct, yet fit, phenotypes is not well understood. In addition, these studies
75 were conducted with a starting strain that was not previously optimized to the growth conditions
76 of the experiment. This confounds the interpretation of the experimental results because
77 adaptations to the growth conditions and loss of the gene occur simultaneously.

78

79 The consequence of the loss of a major metabolic gene can be studied at the systems level
80 through the integration of multi-omics data sets (i.e., metabolomics, fluxomics, proteomics, and
81 transcriptomics) to gain deeper insight into the function of the gene in the context of the
82 biological system as a whole. Previous work has found that the metabolic network is robust to
83 perturbations through adjustments made at the regulatory level that coordinate re-routing of flux
84 with enzyme level (5, 15). While these studies reveal insights to the immediate response of
85 gene loss, the adaptive changes required to overcome the loss were not explored. In addition,
86 improvements in -omics data acquisition and analysis methods could improve and reveal new
87 relationships between changes in -omics data at one layer of the system to another.

88

89 In this study, a combination of experimental design (i.e., starting with a strain that was pre-
90 evolved on glucose M9 minimal media) and systems analysis from multi-omics data was used to
91 mechanistically investigate how multiple phenotypes can overcome the loss of *pgi*. First, the
92 reduction in fitness after the *pgi* KO was found to be attributed to malfunctions in the regulatory
93 and metabolic network that were incapable of handling the redox and glycolytic intermediate
94 metabolite imbalance induced from major shifts in central metabolic flux. Second, all evolved
95 *pgi* KO lineages regained a substantial portion of fitness, but were found have mostly unique

96 genotypes and displayed unique physiologies. Third, the recovery in fitness was enabled by
97 mutations that were selected for by ALE that altered the transcription regulatory network (TRN)
98 and metabolic fluxes to alleviate the redox and sugar phosphate imbalance. These regulatory
99 and metabolic alterations were unique across all endpoints, which lead to the emergence
100 multiple optimal phenotypes.

101 Results

102 Diversity in ALE endpoint phenotypes points to multiple optimal 103 selection outcomes

104 To eliminate the confounding variable of adaptation to the growth conditions of the experiment,
105 a wild-type *E. coli* K-12 MG1655 strain previously evolved under glucose minimal media at
106 37°C(16) (denoted as "Ref") was selected as the starting strain (Fig. 1A). This selection was
107 made to separate changes caused by adaption to the loss of a gene product from those caused
108 by adaption to the growth conditions of the experiment.

109
110 PGI (*pgi*, phosphoglucose isomerase) was removed from Ref to generate strain uPgi (denoted
111 "unevolved *pgi* knockout strain") (Fig. 1B). The loss of *pgi* resulted in an 81% loss in growth
112 rate (Fig. 1 C, D). Eight uPgi independently inoculated starting cultures were simultaneously
113 evolved on glucose minimal media at 37°C in an automated ALE platform (16, 17) denoted
114 "evolved *pgi* knockout strains" or "ePgi" (Fig. 1C). A statistically significant increase in final
115 growth rate (Student's t-test, pvalue<0.05) was found in all ALE endpoints of the ePgi lineages
116 (ave±stdev 284±20% increase in growth rate) compared to uPgi (Fig. 1D). Metabolomics,
117 fluxomics, transcriptomics, genomics, and phenomics data was collected from exponentially
118 growing cultures inoculated in triplicate from Ref, uPgi, and each of the 8 independently evolved
119 end-point lineage populations (ePgi01-08). It is important to note that the data presented below
120 was derived from end-point populations as opposed to isolated clones.

121

122 Statistically significant variability in growth rate, acetate secretion, and glucose uptake rate were
123 found in the ePgi samples (Fig. 1D, Table S1). Specifically, replicates 3, 4, 7, and 8 excreted

124 acetate. Replicate 4, in particular, had acetate secretion levels similar to uPgi, and the highest
125 growth and glucose consumption rate of all endpoints. The overall mutation load also differed
126 across lineages. The overall number of mutations (mutation frequency > 0.2) for each of the
127 end-point replicates were 15, 12, 9, 13, 7, 14, 9, and 7, respectively (Table S7).

128

129 The different phenotypes and genotypes displayed by the end-points raised two defining
130 questions: What metabolic and regulatory changes occurred to allow for a large improvement in
131 fitness without the use of upper glycolysis? How were a diversity of end point physiologies
132 capable of overcoming the loss of PGI? To answer these questions, Intracellular metabolite
133 levels, gene expression levels, and flux levels were measured for the Ref, uPgi strain, and ePgi
134 endpoint populations (Tables S1-7).

135 The PGI KO shifted metabolic flux

136 Genome-scale metabolic flux analysis (MFA) (18) found significant shifts in flux splits throughout
137 central metabolism in response to the loss of PGI (Fig. 2, Table S5). Note that all fluxes
138 discussed in the main text passed observability criteria as described previously (18). Flux splits
139 included the distribution of flux through the oxidative Pentose Phosphate Pathway (oxPPP)
140 (EDD, GND, and PGL), flux through the non-oxidative branch (nonOxPPP), flux around the
141 anaerobic reactions (PPC, PPCK, MALS, ME1, and ME2), flux into the TCA cycle or towards
142 acetate secretion (CS, Ac2rpp, and PDH), and flux through the lower glyoxylate shunt or
143 through the lower TCA cycle (ACONTb, ICDHr, and ICL). A massive increase of over 10,000
144 fold in flux per mol of glucose through the ED Pathway (EDD) was found (note that Ref had only
145 minimal flux through the EDD), while a minor 15.6% drop in flux per mole of glucose through
146 GND was found in uPgi compared to Ref. Redistribution of flux through the nonOxPPP was
147 found. A 79% increase in flux per mole of glucose into the TCA through CS was offset by an

148 87% drop in flux per mole of glucose into the TCA through PPC. A minor 6% drop in acetate
149 secretion per mole of glucose was found. Further, a significant 380.8% increase in flux per
150 mole of glucose through the glyoxylate shunt was found. These changes in major metabolic
151 pathways and flux splits in the cell quantify the magnitude of the perturbation and the initial
152 response of the cell to losing the *pgi* gene function.

153 Perturbed glycolytic intermediates generated a sugar phosphate 154 stress response

155 Shifts in central metabolic fluxes imbalanced central metabolic intermediate metabolite levels
156 leading to a sugar phosphate stress response. LC-MS/MS was used to quantify the absolute
157 metabolite concentrations of glycolytic intermediates, Pentose phosphate pathway (PPP), and
158 TCA cycle intermediates (Table S2); and transcriptomics was used to quantify the relative shifts
159 in genes targeted by transcription factors (Table S2-4). All measured glycolytic and PPP
160 intermediates changed significantly in the uPgi strain as compared to Ref (Fig. 3, Table S2). In
161 particular, an approximate fivefold increase in glucose 6-phosphate (g6p) was found in uPgi
162 compared to Ref (Fig. 4). g6p is the sole substrate of the *pgi* gene. Abnormal elevations in g6p
163 and an imbalance of the glycolytic intermediates in uPgi were found to induce the sugar
164 phosphate toxicity response transcription factor (TF) SgrR(6–8) as measured through the
165 transcriptomic measurements. SgrR is thought to bind hexose phosphates and induce the
166 expression of the small RNA *sgrS* (6–8)(Fig. 4D-E). ePGI strains dampened *sgrS* expression,
167 which was highly overexpressed in uPgi. Further, *SgrS* transcriptionally regulates a number of
168 genes including the *pur* regulon, *ptsG*, and genes involved in biofilm formation and curli
169 formation (7, 8, 19–21).

170 Imbalances in central carbon intermediates induced TRN
171 responses that were consistent with the literature

172 Many *E. coli* TFs are activated by metabolites (22–26). Thus, changes in metabolite levels were
173 investigated to reveal potential TRN responses as measured by changes in expression profiles
174 associated with well-known TF regulons. Many of the measured expression changes appeared
175 to conflict with optimal fitness. Specifically, the *glp* regulon required for glycerol import and
176 catabolism was upregulated by CRP-cAMP(29). cAMP was significantly elevated in the uPGI
177 strain (Supplementary data). This hard-wired regulation led to massive up-regulation of the *glp*
178 regulon in uPgi which could potentially have lead to counterproductive allocation of the
179 proteome to glycerol metabolism.

180

181 Interestingly, the hexose phosphate importer, *uhpT*, was overexpressed in uPgi compared to
182 Ref. High periplasmic g6p plausibly activated the uhpAB two-component system, which in turn
183 up-regulates expression of the hexose phosphate importer *uhpT*(30–32). This result suggests
184 that the concentration build-up in uPgi was so great that g6p spilled over into the periplasmic
185 space(33, 34) (Fig. 3, upper panels). Increased expression of *uhpT* could have generated a
186 loop whereby excessive g6p that spilled into the periplasmic space would be re-imported into
187 the cytosol. The transcriptional attenuation of *ptsG* by *sgrS* may act to compensate for this futile
188 cycle.

189 It should be noted that in the present context, the two examples given above (i.e., the *glp*
190 regulon and g6p cycling) could be considered as counter-productive and not aligning with
191 optimal growth. However, in a different environment, these hard-wired regulatory circuits could
192 play a critical role in maintaining optimal physiology. This provides evidence that the
193 combination of tightly controlled laboratory setting, gene knockout, and multi-omics data

194 collection and analysis described here provided a useful means to reveal these hard wired
195 responses.

196 Imbalances in central carbon intermediates was mirrored in amino 197 acid pools

198 In addition to regulatory shifts, biomass components directly reflected the levels of their
199 biosynthetic precursors (Fig. 3B-C). The aromatic amino acids L-tyrosine (tyr-L), L-
200 phenylalanine (phe-L), and L-tryptophan (trp-L) are derived from phosphoenolpyruvate (pep). A
201 decrease in pep levels in uPgi and and a rise in pep levels in ePgi strains was mirrored by all
202 three of the amino acids (Fig. 3C). An increase in ribose 5 phosphate (r5p) levels in uPgi and
203 ePgi were mirrored by the downstream amino acid L-histidine (his-L) and nucleotide UMP (Fig
204 3B).

205

206 Similar trends were found for amino acid and precursor pairs L-serine (ser-L) and 2-
207 phosphogluconate (2pg), L-aspartate (asp-L) and oxaloacetate (oaa), L-alanine (ala-L) and
208 pyruvate (pyr), and L-glutamate (glu-L), L-glutamine (glu-L), and alpha-ketoglutarate (akg),
209 respectively (Table S2). Perturbations in the distribution and abundance of proteogenic amino
210 acids have been shown to alter protein synthesis rates leading to a drop in the growth rate(35–
211 39). The drop in the growth rate of the uPgi strain and regain of fitness in the ePgi strains
212 provide evidence that an imbalance in glycolytic intermediates directly alters growth rate via
213 manipulating proteogenic amino acid levels.

214

215 The regulatory response to elevated g6p levels and the relationship between biomass
216 components and their precursors reflected the importance of balancing glycolytic, PPP, and

217 TCA cycle intermediates to maintain balanced ratios of amino acids levels for protein
218 biosynthesis and purine/pyrimidine mono-nucleotides for nucleotide biosynthesis.

219

220 Mutations that targeted alternative glucose import systems
221 corrected TRN responses, and helped to rebalance glycolytic
222 intermediate levels

223 Major alterations in expression profiles were found in the evolved KO strains that correlated well
224 with mutations detected in TFs. These included mutations to *galR* (Fig. 5) and *malT* (Fig. 6) in
225 the ePgi strains. A 22 nucleotide deletion in the small molecule binding domain of *galR* in
226 ePgi07 appears to negate repression of *galR* controlled operons (Fig. 5). These include
227 *galETKM*, *galP*, and *mgIBAC* that encode enzymes for galactose catabolism, symport, and ABC
228 transport, respectively(40). These operons are also regulated by CRP-cAMP, and were not
229 expressed in Ref. The galactose importers have lesser affinity for the transport of glucose,
230 which may give ePgi07 an additional route to import and catabolize glucose from the
231 environment. In addition, the mutation may have aided in conserving pep for aromatic amino
232 acid production, which was limiting fitness in all of the pgi strains (as discussed previously).

233

234 In another example, a mobile element insertion (MOB) that truncated the MalT TF in ePgi06
235 was found that appeared to silence expression of MalT(41) controlled operons (Fig. 6). The
236 MOB introduced a stop codon that truncated the MalT peptide from 901 amino acids to 29
237 amino acids. All binding-domains and catalytic sites were cleaved(42, 43). MalT controlled
238 genes are involved in glycogen turnover, and may give ePgi06 an advantage in controlling the
239 levels of hexose phosphates that are converted to and broken down from glycogen.

240 An imbalance in redox carriers was compensated for by shifts in
241 hydrogenase flux and buffered by glutathione

242 Genome-scale MFA(18) confirmed that removal of the *pgi* gene diverted all upper glycolytic flux
243 into the oxidative pentose phosphate pathway (oxPPP) (Fig. 2). The loss of PGI resulted in a
244 556.7% increase in flux per mol of glucose towards the oxPPP in uPgi (14.4 and 94.7% flux per
245 mol of glucose in ref and uPgi, respectively). Note that as discussed previously, a large portion
246 of the flux into the oxPPP was diverted down the ED pathway after the first NADPH generating
247 step to avoid generating additional NADPH via the second NADPH generating step of the
248 oxPPP (Fig. 2). Rearrangement of flux through hydrogenases to compensate for the increased
249 flux towards NADPH generation were found (Fig. 2). Notable is the reversed utilization of the
250 transhydrogenases from net NADPH to NADH generation in uPgi and ePgi strains
251 (approximately -8 fold change in uPgi and ePgi strains in NADPH generation through THD2pp,
252 and -3 fold change in uPgi and -1 to 4 fold change in ePgi strains in NADH generation through
253 NADTRHD). Other hydrogenases significantly altered include serine dehydrogenase (LSERDHR,
254 note the altered levels of ser-L mentioned previously), as well as isocitrate dehydrogenase
255 (ICD) and glutamate synthase (GLUSy, note the altered levels of akg, gln-L, and glu-L
256 mentioned previously).

257

258 The increased flux through the oxPPP would generate an increased abundance of NADPH and
259 thus a redox imbalance. LC-MS/MS(44) was used to quantify the absolute metabolite
260 concentrations of the redox carriers. While major shifts in the redox carriers were found (Fig.
261 3A), a statistically significant change in NADPH between Ref and uPgi was not found.
262 However, statistically significant changes in NADP and reduced and oxidized Glutathione were
263 found. This indicates a potential rapid buffering of NADPH by the Glutathione via glutathione
264 reductase (GTHOr) (Fig. 3A).

265 High NADPH promoted activation of oxidative stress responders

266 Mutations in *soxR* in ePgi02 and *rseC* in ePgi01 were found that altered the expression of
267 oxidative stress genes (Fig. 7). The *soxR* mutation truncated the Fe-S cluster binding site of the
268 SoxR peptide by introducing a premature stop codon (Fig. 7C). Cleavage of the Fe-S cluster
269 does not affect DNA-binding, but transcriptional activation of target genes *soxS* and *fumC* and
270 transcriptional deactivation of *soxR* are impaired(45–47). *soxR* was up-regulated in ePgi02,
271 which indicated that the mutation negated *soxR*'s self-regulation.

272

273 The *rseC* single nucleotide deletion introduced a frameshift that truncated a large portion of the
274 transmembrane helix region starting several amino acids from the initial deletion (Fig. 7D) that
275 may affect R_{sox}-R_{seC} complex formation or activity. *rseC* mutants were found previously to
276 exhibit constitutive *soxS* expression by preventing the R_{sox}-R_{seC} complex to inhibit reduction
277 and inactivation of SoxR(48) (Fig. 7A). *soxS*, as well as many of its downstream activation
278 targets including *acrA*, *acrB*, *fldA*, *fpr*, *inaA*, and *sodA*, were up-regulated in ePgi01, which
279 indicated that the mutation promotes expression of *soxS*. The R_{sox}-R_{seC} complex prevents
280 reduction and inactivation of SoxR(48).

281 Mutations in transhydrogenases helped to alleviate redox 282 imbalance

283 Mutations selected during adaptive evolution also introduced innovations that targeted
284 metabolic network elements involved in NADPH production. Mutated transhydrogenases
285 included *sthA*, *pntB*, *icd*, and *zwf*. The soluble and membrane bound transhydrogenases act to
286 interconvert NADP(H) and NAD(H) (49, 50) (Fig. 8). Mutations in the soluble *sthA* (49) and
287 membrane bound *pntB* (50) transhydrogenases in ePgi07 and ePgi04, respectively, were found

288 (Fig. 8). The *sthA* mutation appeared near the dimerization domain, and may affect enzyme
289 complex formation. The *pntB* mutation appeared in the transmembrane region, and may affect
290 catalytic activity or membrane association. It has been demonstrated that altered activity of
291 *sthA* and *pntAB* confers a fitness advantage in *pgi* mutant strains by rebalancing the ratios of
292 NADH to NADPH (49, 50). Interestingly, mutations in *sthA* and *pntB* were selected for in
293 previous evolutions of a *pgi* strain (3). This observation provides further evidence that the *sthA*
294 and *pntB* mutations provided a fitness advantage to ePgi07 and ePgi04 by rebalancing the
295 ratios of NADH to NADPH via modulating the activity of the transhydrogenases. Note that
296 ePgi07 and ePgi04 were also found to have the highest increase in flux through the soluble
297 transhydrogenases.

298

299 Isocitrate dehydrogenase (ICD) catalyzes the conversion of isocitrate (*icit*) to 2-oxoglutarate
300 (*akg*) while reducing NADP⁺ to NADPH (Fig. 9). Activity of ICD also regulates the flux split
301 between the full TCA cycle and the glyoxylate shunt(51–53). A point mutation at the 395
302 residue that changed the amino acid from positively charged (L-arginine) to negatively charged
303 (L-cysteine) in ICD was found in all ePgi replicates except replicate 7 (Fig 9). The mutation
304 occurs 4 Angstroms from the phosphate moiety of NADP. The 395 residue has been shown to
305 be directly involved in NADP-binding (54), and appears to allow the mutated enzyme to either
306 utilize NAD as a cofactor or exclude NADPH from the active site by like charge repulsion. The
307 mutation was found to redirect flux through the glyoxylate shunt instead of the TCA cycle, and
308 may provide a fitness advantage to the ePgi strains by limiting the production of NADPH in the
309 TCA cycle.

310

311 Metabolome, fluxome, transcriptome, and genome were unique in
312 each ePgi strain

313 While the ePgi strains were not able to recover the fitness of Ref, they were able to recover the
314 initial growth rate of wild-type MG1655. Many intermediate and cofactor levels, including g6p,
315 remained perturbed in ePgi strains to varying degrees. However, the majority of initially
316 elevated transcription involving sugar phosphate stress, carbon catabolite repression, the *uhpT*
317 transporter, and other general stress responders in uPgi were dampened or completely shut
318 down in ePgi strains. This indicated that the TRN had evolved to cope with the changed
319 metabolome. Many of these changes to the TRN could be directly attributed to mutations.

320

321 The recovery to wild-type levels was in part made possible by a complete rewiring of central
322 carbohydrate metabolic flux splits (Fig. 3). The rewiring differed substantially between ePgi
323 strains. While an increase in flux through GND and a decrease in flux through the ED pathway
324 occurred in all ePgi endpoints, the flux through each pathway differed substantially. GND flux
325 varied from 389.9 to 604.6% increase per mol glucose compared to Ref, and ED pathway flux
326 varied from 150.9 to 4463.8% increase per mol glucose compared to Ref. NonOxPPP flux
327 varied substantially among the strains, even altering between net forward and reverse utilization
328 of TALA. Of particular note, flux through PPC was regained in ePgi04 and ePgi07, and flux
329 through the glyoxylate shunt was lost in ePgi07. The later differences in particular correlate with
330 mutations in the transhydrogenases and *ica*, respectively.

331

332 Conclusion

333 Loss of *pgi* induced massive perturbations to the metabolome, fluxome, and transcriptome in *E.*
334 *coli*, and led to a greatly retarded post knockout growth rate. In contrast to previous work (5), it
335 was found that the loss of *pgi* induced major changes in all -omics data measured not just local
336 to the perturbation, but in distal network locations. Flux rerouting to compensate for the loss of
337 *pgi* imbalanced the PPP and glycolytic intermediate levels, which lead to a sugar phosphate
338 stress response. The deleterious effects of this response were attributed to a misallocation of
339 protein, a deleterious cycle of re-import of hexose phosphate, and alterations in the distributions
340 and amount of proteogenic amino acids and nucleotides. Redistribution of glycolytic flux into
341 the oxPPP generated an overabundance of NADPH, which led to a redox imbalance.

342
343 ALE selected for mutations that helped to alleviate redox and glycolytic intermediate
344 imbalances. Differences in the metabolome and mutation landscape led to a diversity of
345 expression and fluxome profiles in ePgi strains. The multitude of hydrogenases and routes to
346 generate glycolytic intermediates allowed for regulatory and metabolic flexibility in overcoming
347 redox and glycolytic intermediate imbalance. Finally, the diversity in fixed mutations and the
348 concomitant emergence of multiple optimal phenotypes was a manifestation of this metabolic
349 flexibility. Additional studies utilizing ALE to uncover the response of a cell to a major network
350 perturbation are likely to uncover additional mechanisms available to biological networks to
351 overcome such major perturbations.

352

Contributions

D.M. designed the experiments; generated the strains; conducted all aspects of the metabolomics, fluxomics, phenomics, transcriptomics, and genomics experiments; performed all multi-omics statistical, graph, and modeling analyses; and wrote the manuscript. T.E.S. ran the ALE experiments. E.B. assisted with structural analysis. R.S. processed the DNA and RNA samples. S.X. assisted with metabolomics and fluxomics data collection, sample processing, and peak integration. Y.H. assisted with fluxomics data collection and sample processing. A.M.F designed and supervised the evolution experiments, and contributed to the data analysis and the manuscript. B.O.P conceived and outlined the study, supervised the data analysis, and co-wrote the manuscript.

366 Acknowledgements

367 We thank José Utrilla for helpful discussion and guidance when implementing the knockouts in
368 the pre-evolved strain. We thank Jamey Young for helpful discussions throughout the MFA
369 analysis. We thank Laurence Yang for helpful discussions regarding optimization and statistical
370 analysis. This work was funded by the Novo Nordisk Foundation Grant Number
371 NNF10CC1016517.

372

373 **Competing financial interests**

374 The authors declare no competing financial interests.

375

376 Figures

377 Fig. 1

378 Evolution of knockout (KO) strains from a pre-evolved (i.e., optimized) wild-type strain. A) Wild-
379 type (wt) *E. coli* (MG1655 K-12) was previously evolved on glucose minimal media at 37°C(16).
380 An isolate from the endpoint of the evolutionary experiment was selected as the starting strain
381 for subsequent KO of *pgi* and adaptive laboratory evolution (ALE). B) Adaptive laboratory
382 evolution trajectories of the evolved knockout lineages. -Omics data collected from the fresh
383 KO, and end-point lineages included metabolomics, fluxomics, physiology, DNA resequencing,
384 and transcriptomics. C) Phosphoglucose isomerase (PGI) was disabled by the gene KO. PGI
385 is the first step in glycolysis and converts glucose 6 phosphate (g6p) to fructose 6 phosphate
386 (f6p). D) Growth rate and glucose (glc-D) uptake and acetate (ac) excretion rates for
387 unevolved KO (uPgi) and evolved KOs (ePgi). Error bars denote 95% confidence intervals from
388 biological triplicates.

389 Fig. 2

390 Changes in flux splits pre- and post- adaptive evolution. A) Network diagram with reactions
391 involved in flux splits annotated. Reactions included phosphogluconate dehydratase (EDD), 6-
392 phosphogluconate dehydrogenase (GND), 6-phosphogluconolactonase (PGL), phosphoenol
393 pyruvate carboxylase (PPC), phosphoenolpyruvate carboxylase kinase (PPCK), malate
394 dehydrogenase (MALS), NADP-dependent malic enzyme (ME1), NAD-dependent malic enzyme
395 (ME2), citrate synthase (CS), acetate secretion (ACT2rpp), pyruvate dehydrogenase (PDH),
396 aconitase (ACONTb), isocitrate dehydrogenase (ICDHyr), and isocitrate lyase (ICL). B)

397 Measured absolute fluxes for Ref, uPgi, and ePgi strains. Values are derived from averages
398 taken from triplicate cultures that were analyzed in duplicate (n=6).

399

400 Fig. 3

401 An imbalance in redox carriers. A) Box and whiskers plots of log-normalized absolute
402 metabolite levels ($\mu\text{mol} \cdot \text{gDCW}^{-1} \cdot \text{h}^{-1}$) of the redox carriers NAD(P)(H) and the reduced (gthrd)
403 and oxidized (gthox) Glutathiones. Network diagram of the interconversion of nadh to nad, nadp
404 to nadph, and gthox and nadph to gthrd and nadp. An imbalance in glycolytic and PPP
405 intermediates, and their downstream biosynthetic components. B) Schematic of the connection
406 between the PPP precursor ribose 5 phosphate (r5p) and downstream amino acid and
407 nucleotides L-histidine (his-L), Inosine Monophosphate (IMP), and Uridine Monophosphate
408 (UMP). Box and whiskers plots of absolute metabolite levels of r5p, his-L, imp, and ump. C)
409 Schematic of the connection between the glycolytic precursor Phosphoenol Pyruvate (pep) and
410 downstream aromatic amino acids L-Tryptophan (trp-L), L-Tyrosine (tyr-L), and L-Phenylalanine
411 (phe-L). Box and whiskers plots of pep, trp-L, tyr-L, and phe-L. Values are derived from
412 averages taken from triplicate cultures that were analyzed in duplicate (n=6).

413

414 Fig. 4

415 KO of PGI led to a hexose phosphate toxicity response. The magnitude of g6p in the initial
416 knockout led to a deleterious cycle whereby leakage of hexose phosphate across the inner
417 membrane (33, 34) induced hexose phosphate re-uptake via the uhpBC two-component system
418 and *uhpT* hexose phosphate transporter (30–32). A) A network map and regulatory schematic
419 of the reactions into and out of the g6p node. The reaction in red is removed through the PGI

420 KO. B) A mechanistic schematic of the uhpBC two-component system that sensed periplasmic
421 hexose phosphate. The transcription factor UphA positively upregulated the expression of the
422 hexose phosphate importer uhpT. C) Metabolite, expression, and flux levels near the node of
423 perturbation. Abnormal elevations in glucose 6-phosphate (g6p) and imbalance of the glycolytic
424 intermediates in *pgi* were found to induce a sugar phosphate toxicity response sensed through
425 *sgrR* and mediated through the action of the small RNA *sgrS* (6–8) (Panels A-B). D-E)
426 Regulatory schematic of *sgrR* and *sgrST-setA* operons. Regulatory schematic of genes
427 subjected to transcriptional activation or attenuation by the small RNA *sgrS* (7, 20, 55, 56). F)
428 Gene expression profiles of sugar phosphate response genes. Note the elevations in g6p and
429 corresponding upregulation of *sgrS* in response to activation of *SgrR* by g6p that is consistent
430 with the literature (7, 20, 55, 56). Metabolite concentrations are derived from averages taken
431 from triplicate cultures that were analyzed in duplicate (n=6). Gene expression values are
432 derived from averages of biological duplicates.

433 Fig. 5

434 An inframe 33 nucleotide deletion (DEL) that removed 11 amino acids in the small molecule
435 binding domain of *galR* negates *galR* repression in ePgi07 (Panels A-C). A) Regulatory network
436 specifically controlled by cAMP-CRP, *galR*, and *galS* (57–59). cAMP-CRP can both positively
437 and negatively regulate the expression of *galR*, *galS*, *galETKM*, *galP*, and *mgIBAC*; *GalR* and
438 *GalS* act as repressors; and *GalR* and *GalS* bound to galactose active primarily as activators.
439 B) Crystal structure of the *galR* transcription factor (60). The position of the deletion is
440 highlighted in red, the small molecule binding domain is highlighted in cyan, and the H-T-H
441 DNA-binding region is highlighted in magenta. C) Mutation frequency for *galR*, metabolite
442 concentration for cAMP, and expression profiles of *galR* controlled operons. Note the increased
443 expression of *galP* and *galETKM* in ePgi07. Metabolite concentrations are derived from

444 averages taken from triplicate cultures that were analyzed in duplicate (n=6). Gene expression
445 values are derived from averages of biological duplicates.

446

447 Fig. 6

448 A mobile element insertion (MOB) that truncated the MalT TF in ePgi06 was found that
449 appeared to silence expression of MalT controlled operons. A) Schematic of the malT
450 operon(41) and truncated malT peptide. The mobile element insertion introduced a stop codon
451 that reduced the MalT peptide from 901 amino acids to 29 amino acids. All binding-domains
452 and catalytic sites were cleaved (42, 43). B) Operons controlled by malT(41). All regulators
453 except malT and CRP-cAMP have been omitted. MalT controlled genes are involved in
454 glycogen turnover, and may give ePgi06 an advantage in controlling the levels of hexose
455 phosphates that are converted to and broken down from glycogen. C) Mutation frequency of
456 malT, metabolite concentration for cAMP, and expression profiles for malT and malT regulated
457 genes. Note the significantly repressed gene expression levels of MalT controlled genes in
458 ePgi06. Metabolite concentrations are derived from averages taken from triplicate cultures that
459 were analyzed in duplicate (n=6). Gene expression values are derived from averages of
460 biological duplicates.

461 Fig. 7

462 Mutations in *soxR* and *rseC* that altered the expression of oxidative stress genes. A) protein-
463 protein interaction schema between SoxR and RseC. In the reduced form, the iron sulfur
464 clusters of the SoxR homodimers sense the presence of free radicals and ROS(61, 62). The
465 oxidation of the iron sulfur clusters by free radicals and ROS induces a conformation changes
466 from the inactive form to the active form(63). While both reduced and inactive form and

oxidized and active forms of SoxR are capable of binding DNA, only the active form is capable of activating or inhibiting transcription(45, 64–67). The R_{sox}-R_{seC} complex prevents reduction and inactivation of SoxR(48). B) Regulatory schematic of a subset of SoxR and SoxS controlled operons. C) Crystal structure of SoxR (68). The *soxR* SNP eliminated the Fe-S cluster binding site of the SoxR peptide. The SoxR DNA-binding region in proximity to single stranded DNA (ssDNA) is shown below. D) Crystal structure of *rseC*. The *rseC* mutation cleaved a large portion of the transmembrane helix region that may affect R_{sox}-R_{seC} complex formation or activity. The mutated and/or cleaved residues are shown in red. E) Mutation frequency and gene expression profiles. Gene expression values are derived from averages of biological duplicates.

Fig. 8

Mutations in the soluble *sthA* (49) and membrane bound *pntB* (50) transhydrogenases that potentially aid in balancing NAD(P)(H) cofactors. A) Schematic of the *sthA* and *pntAB* operons. B) Network diagrams of the soluble pyridine nucleotide transhydrogenase (NADTRHD) reaction catalyzed by *sthA* and the membrane bound pyridine nucleotide transhydrogenase (THD2pp) reaction catalyzed by *pntAB*. C) Mutation frequency and metabolite and expression levels near the genes. D) The *sthA* mutation in ePgi04 appeared near the dimerization domain, and may affect enzyme complex formation. E) The *pntB* mutation in ePgi07 appeared in the transmembrane region, and may affect catalytic activity or membrane association. It has been demonstrated that altered activity of *sthA* and *pntAB* confers a fitness advantage in *pgi* mutant strains by rebalancing the ratios of NADH to NADPH (49, 50). Metabolite concentrations are derived from averages taken from triplicate cultures that were analyzed in duplicate (n=6). Gene expression values are derived from averages of biological duplicates.

491 Fig. 9

492 A beneficial mutation that rewired the TCA cycle via a cofactor usage swap in isocitrate
 493 dehydrogenase (ICD) aided in alleviating the excessive conversion of NADP to NADPH. A)
 494 Network schematic of a segment of the TCA cycle. The reaction in red is catalyzed by ICD. B)
 495 Crystal structure of ICD. The mutated amino acids are highlighted in yellow. C) Zoom in on the
 496 active site of isocitrate dehydrogenase showing the proximity of the mutated amino acid to the
 497 phosphate group of NADP. The mutation occurs 4 Angstroms from the phosphate moiety of
 498 NADPH. The 395 residue has been shown to be directly involved in NADPH-binding (54), and
 499 appears to allow the mutated enzyme to utilize NADH as a cofactor. D) Mutation frequency and
 500 metabolite, expression, and flux levels near the mutated gene. System components near the
 501 ICDHyr reaction in the ICD mutant strains are significantly changed. Metabolite concentrations
 502 are derived from averages taken from triplicate cultures that were analyzed in duplicate (n=6).
 503 Flux levels are derived from averages taken from triplicate cultures that were analyzed in
 504 duplicate (n=6). Gene expression values are derived from averages of biological duplicates.
 505

506 Tables

507 Table 1

508 List of primers used to generate the KO strains in this study.

strain	primer	name	sequence (HPLC)	primer	name	sequence
pgl	F_KO_primer	pgl_F_KO_primer	ACAATTCTCAAAATCAGAAGAGTATTGCTAatgAAAAACATCAATCCAACGCAGACCGCTattccgggatcgtcgacc	conf_primF	conf_pri	AGCGGGGCGGTTGTCAACGA
pgl	R_KO_primer	pgl_R_KO_primer	CGCCTTATCCGGCCTACATATCGACGATGAttaACCGCGCCACGCTTTATAGCGGTTAATgtgtaggctggagctgcttc	conf_primR	conf_pri	TTTATCTGATAAAAAATGC

510

511 Supplemental Tables:

512 Table S1:

513 Average growth rates, substrate uptake and secretion rates of the initial knockout strains and
514 evolved endpoints grown in biological triplicate and sample during exponential growth. The
515 95% confidence intervals (denoted “lb” and “ub”) are shown.

516

517 Table S2:

518 Absolute metabolite concentrations for all ref, uKO, and eKO strains in the study. Data is
519 presented in units of GLog normalized $\mu\text{mol} \cdot \text{gDCW}^{-1}$ and height ratio (for components without a
520 calibration curve). Table headers include the following (from left to right): 1) the component
521 name (i.e., MRM transition used to identify the respective metabolite). 2) The statistical
522 imputation method used to impute missing replicates. Imputation methods included
523 “mean_fature” (the mean of all detected replicates) and “Ameliall”. 3) The name of the sample
524 and replicate. 4) The units of the measurement. 5) The value of the measurement. 6) The
525 metabolite abbreviations. All metabolite abbreviations match BiGG identifiers for the iJO1366
526 model of *E. coli*.

527

528 Table S3:

529 Gene expression differences for all ref, uKO, and eKO strains in the study. The table header
530 nomenclature follows the identifiers described in Cuffdiff. To summarize, table headers include
531 the following (from left to right): 1) and 2) the gene identifier used by Bowtie. 3) The name of

the gene. 4) The name of the reference sample that the comparison was made against. 5) The name of the sample that was compared to the reference sample. 6) That status of the analyzed value. A status of "OK" indicates sufficient coverage. 7) and 8) the average gene expression value found for sample 1 and 2, respectively. 9) The fold change. 10) The value of the test statistic used by Cuffdiff. 11) The significance value of the fold change. 12) The corrected significance value of the fold change. 12) Whether the gene expression difference is significant. A q_value less than 0.05 was considered significant.

Table S4:

Gene expression normalized counts for all ref, uKO, and eKO strains in the study. The table header nomenclature follows the identifiers described in Cuffnorm. To summarize, table headers include the following (from left to right): 1) The name of the sample grouping used in the normalization. 2) The name of the sample. 3) The tracking id used by Cuffnorm. 4) The gene id used by Cuffnorm. 5) The name of the gene. 6) The gene locus identifier used by Bowtie. 7) The normalized value.

Table S5:

Absolute metabolic flux values for all ref, uKO, and eKO strains in the study. Table headers include the following (from left to right): 1) The name of the MFA simulation (i.e., sample name). 2) The reaction abbreviation. All reaction abbreviations follow the BiGG identifiers for iJO1366, and can be found in table S7. 3) The flux units. 4) The number of points sampled. 5), 6), 7), and 8) The average, variation, and 95% confidence intervals for the sampled fluxes. 9) The confidence bounds used for sampling. 10), 11), 12), 13), and 14) The minimum, maximum, median, and interquartile ranges for the sampled fluxes.

555 **Table S6:**

556 Metabolic model used for MFA and sampling simulations. Table headers include the following
557 (from left to right): 1) The reaction abbreviation. All reaction abbreviations follow the BiGG
558 identifiers for iJO1366. 2) The reaction equation and MFA carbon mapping for all reactions. All
559 metabolite abbreviations follow the BiGG identifiers for iJO1366.

560 **Table S7:**

561 Annotated mutations. Table headers include the following (from left to right): 1) The type of
562 mutation. Mutations include amplification (AMP), deletion (DEL), insertions (INS), mobile
563 element aided insertions or deletions (MOB), single nucleotide polymorphism (SNP). 2) The
564 frequency of the mutation in the end point lineage population. 3) The genes affected by the
565 mutations. Mutations located in an intergenic region between two genes are shown with both
566 genes separated by a semi-colon. 4) The annotation for the mutation. 5) The starting position
567 of the mutation on the chromosome. 6) The name of the end-point lineage. 7) The location of
568 the mutation. Locations include coding regions, regions associated with cryptic prophages,
569 intergenic regions, regions two coding genes not classified as an intergenic region
570 (intergenic/intergenic), and repetitive elements (REP or RIP). 7) The chromosome number of
571 the mutation. In this case, 1 for all strains because *E. coli* has only one chromosome.

572

573

References

1. Usui Y, Hirasawa T, Furusawa C, Shirai T, Yamamoto N, Mori H, Shimizu H. 2012. Investigating the effects of perturbations to *pgi* and *eno* gene expression on central carbon metabolism in *Escherichia coli* using (^{13}C) metabolic flux analysis. *Microb Cell Fact* 11:87.
2. Ahn J, Chung BKS, Lee D-Y, Park M, Karimi IA, Jung J-K, Lee H. 2011. NADPH-dependent *pgi*-gene knockout *Escherichia coli* metabolism producing shikimate on different carbon sources. *FEMS Microbiol Lett* 324:10–16.
3. Charusanti P, Conrad TM, Knight EM, Venkataraman K, Fong NL, Xie B, Gao Y, Palsson BØ. 2010. Genetic basis of growth adaptation of *Escherichia coli* after deletion of *pgi*, a major metabolic gene. *PLoS Genet* 6:e1001186.
4. Fong SS, Nanchen A, Palsson BO, Sauer U. 2006. Latent pathway activation and increased pathway capacity enable *Escherichia coli* adaptation to loss of key metabolic enzymes. *J Biol Chem* 281:8024–8033.
5. Ishii N, Nakahigashi K, Baba T, Robert M, Soga T, Kanai A, Hirasawa T, Naba M, Hirai K, Hoque A, Ho PY, Kakazu Y, Sugawara K, Igarashi S, Harada S, Masuda T, Sugiyama N, Togashi T, Hasegawa M, Takai Y, Yugi K, Arakawa K, Iwata N, Toya Y, Nakayama Y, Nishioka T, Shimizu K, Mori H, Tomita M. 2007. Multiple high-throughput analyses monitor the response of *E. coli* to perturbations. *Science* 316:593–597.
6. Richards GR, Patel MV, Lloyd CR, Vanderpool CK. 2013. Depletion of glycolytic intermediates plays a key role in glucose-phosphate stress in *Escherichia coli*. *J Bacteriol* 195:4816–4825.
7. Vanderpool CK, Gottesman S. 2004. Involvement of a novel transcriptional activator and small RNA in post-transcriptional regulation of the glucose phosphoenolpyruvate

- 597 phosphotransferase system. *Mol Microbiol* 54:1076–1089.
- 598 8. Vanderpool CK, Gottesman S. 2007. The novel transcription factor SgrR coordinates the
599 response to glucose-phosphate stress. *J Bacteriol* 189:2238–2248.
- 600 9. Holmgren A. 1976. Hydrogen donor system for *Escherichia coli* ribonucleoside-diphosphate
601 reductase dependent upon glutathione. *Proceedings of the National Academy of Sciences*
602 73:2275–2279.
- 603 10. Lin Z, Xu Z, Li Y, Wang Z, Chen T, Zhao X. 2014. Metabolic engineering of *Escherichia coli*
604 for the production of riboflavin. *Microb Cell Fact* 13:104.
- 605 11. Tenaillon O, Barrick JE, Ribick N, Deatherage DE, Blanchard JL, Dasgupta A, Wu GC,
606 Wielgoss S, Cruveiller S, Médigue C, Schneider D, Lenski RE. 2016. Tempo and mode of
607 genome evolution in a 50,000-generation experiment. *Nature* 536:165–170.
- 608 12. Pluain J, Hindré T, Le Gac M, Tenaillon O, Cruveiller S, Médigue C, Leiby N, Harcombe
609 WR, Marx CJ, Lenski RE, Schneider D. 2014. Epistasis and Allele Specificity in the
610 Emergence of a Stable Polymorphism in *Escherichia coli*. *Science* 343:1366–1369.
- 611 13. Dragosits M, Mattanovich D. 2013. Adaptive laboratory evolution -- principles and
612 applications for biotechnology. *Microb Cell Fact* 12:64.
- 613 14. Chou H-H, Marx CJ, Sauer U. 2015. Transhydrogenase promotes the robustness and
614 evolvability of *E. coli* deficient in NADPH production. *PLoS Genet* 11:e1005007.
- 615 15. Nakahigashi K, Toya Y, Ishii N, Soga T, Hasegawa M, Watanabe H, Takai Y, Honma M,
616 Mori H, Tomita M. 2009. Systematic phenome analysis of *Escherichia coli* multiple-
617 knockout mutants reveals hidden reactions in central carbon metabolism. *Mol Syst Biol*
618 5:306.

- 619 16. LaCroix RA, Sandberg TE, O'Brien EJ, Utrilla J, Ebrahim A, Guzman GI, Szubin R, Palsson
620 BO, Feist AM. 2015. Use of Adaptive Laboratory Evolution To Discover Key Mutations
621 Enabling Rapid Growth of *Escherichia coli* K-12 MG1655 on Glucose Minimal Medium.
622 *Appl Environ Microbiol* 81:17–30.
- 623 17. Sandberg TE, Pedersen M, LaCroix RA, Ebrahim A, Bonde M, Herrgard MJ, Palsson BO,
624 Sommer M, Feist AM. 2014. Evolution of *Escherichia coli* to 42 °C and subsequent genetic
625 engineering reveals adaptive mechanisms and novel mutations. *Mol Biol Evol* 31:2647–
626 2662.
- 627 18. McCloskey D, Young JD, Xu S, Palsson BO, Feist AM. 2016. Modeling Method for
628 Increased Precision and Scope of Directly Measurable Fluxes at a Genome-Scale. *Anal*
629 *Chem* 88:3844–3852.
- 630 19. Bak G, Lee J, Suk S, Kim D, Young Lee J, Kim K-S, Choi B-S, Lee Y. 2015. Identification of
631 novel sRNAs involved in biofilm formation, motility, and fimbriae formation in *Escherichia*
632 *coli*. *Sci Rep* 5:15287.
- 633 20. Kimata K, Tanaka Y, Inada T, Aiba H. 2001. Expression of the glucose transporter gene,
634 *ptsG*, is regulated at the mRNA degradation step in response to glycolytic flux in
635 *Escherichia coli*. *EMBO J* 20:3587–3595.
- 636 21. Vanderpool CK. 2007. Physiological consequences of small RNA-mediated regulation of
637 glucose-phosphate stress. *Curr Opin Microbiol* 10:146–151.
- 638 22. Gama-Castro S, Salgado H, Santos-Zavaleta A, Ledezma-Tejeda D, Muñoz-Rascado L,
639 García-Sotelo JS, Alquicira-Hernández K, Martínez-Flores I, Pannier L, Castro-Mondragón
640 JA, Medina-Rivera A, Solano-Lira H, Bonavides-Martínez C, Pérez-Rueda E, Alquicira-
641 Hernández S, Porrón-Sotelo L, López-Fuentes A, Hernández-Koutouchewa A, Del Moral-

- 642 Chávez V, Rinaldi F, Collado-Vides J. 2016. RegulonDB version 9.0: high-level integration
643 of gene regulation, coexpression, motif clustering and beyond. *Nucleic Acids Res* 44:D133–
644 43.
- 645 23. Cho S, Cho Y-B, Kang TJ, Kim SC, Palsson B, Cho B-K. 2015. The architecture of ArgR-
646 DNA complexes at the genome-scale in *Escherichia coli*. *Nucleic Acids Res* 43:3079–3088.
- 647 24. Federowicz S, Kim D, Ebrahim A, Lerman J, Nagarajan H, Cho B-K, Zengler K, Palsson B.
648 2014. Determining the control circuitry of redox metabolism at the genome-scale. *PLoS*
649 *Genet* 10:e1004264.
- 650 25. Kim D, Hong JS-J, Qiu Y, Nagarajan H, Seo J-H, Cho B-K, Tsai S-F, Palsson BØ. 2012.
651 Comparative analysis of regulatory elements between *Escherichia coli* and *Klebsiella*
652 *pneumoniae* by genome-wide transcription start site profiling. *PLoS Genet* 8:e1002867.
- 653 26. Cho B-K, Federowicz S, Park Y-S, Zengler K, Palsson BØ. 2011. Deciphering the
654 transcriptional regulatory logic of amino acid metabolism. *Nat Chem Biol* 8:65–71.
- 655 27. You C, Okano H, Hui S, Zhang Z, Kim M, Gunderson CW, Wang Y-P, Lenz P, Yan D, Hwa
656 T. 2013. Coordination of bacterial proteome with metabolism by cyclic AMP signalling.
657 *Nature* 500:301–306.
- 658 28. Hermesen R, Okano H, You C, Werner N, Hwa T. 2015. A growth-rate composition formula
659 for the growth of *E. coli* on co-utilized carbon substrates. *Mol Syst Biol* 11:801.
- 660 29. Larson TJ, Cantwell JS, van Loo-Bhattacharya AT. 1992. Interaction at a distance between
661 multiple operators controls the adjacent, divergently transcribed *glpTQ-glpACB* operons of
662 *Escherichia coli* K-12. *J Biol Chem* 267:6114–6121.
- 663 30. Weston LA, Kadner RJ. 1988. Role of *uhp* genes in expression of the *Escherichia coli*

- 664 sugar-phosphate transport system. *J Bacteriol* 170:3375–3383.
- 665 31. Dahl JL, Wei BY, Kadner RJ. 1997. Protein phosphorylation affects binding of the
666 *Escherichia coli* transcription activator UhpA to the uhpT promoter. *J Biol Chem* 272:1910–
667 1919.
- 668 32. Maloney PC, Ambudkar SV, Anatharam V, Sonna LA, Varadhachary A. 1990. Anion-
669 exchange mechanisms in bacteria. *Microbiol Rev* 54:1–17.
- 670 33. Bolten CJ, Kiefer P, Letisse F, Portais J-C, Wittmann C. 2007. Sampling for metabolome
671 analysis of microorganisms. *Anal Chem* 79:3843–3849.
- 672 34. Link H, Anselment B, Weuster-Botz D. 2008. Leakage of adenylates during cold
673 methanol/glycerol quenching of *Escherichia coli*. *Metabolomics* 4:240–247.
- 674 35. Stoebel DM, Dean AM, Dykhuizen DE. 2008. The cost of expression of *Escherichia coli* lac
675 operon proteins is in the process, not in the products. *Genetics* 178:1653–1660.
- 676 36. Kaleta C, Schäuble S, Rinas U, Schuster S. 2013. Metabolic costs of amino acid and
677 protein production in *Escherichia coli*. *Biotechnol J* 8:1105–1114.
- 678 37. Traxler MF, Chang D-E, Conway T. 2006. Guanosine 3',5'-bispyrophosphate coordinates
679 global gene expression during glucose-lactose diauxie in *Escherichia coli*. *Proc Natl Acad*
680 *Sci U S A* 103:2374–2379.
- 681 38. Tao H, Bausch C, Richmond C, Blattner FR, Conway T. 1999. Functional genomics:
682 expression analysis of *Escherichia coli* growing on minimal and rich media. *J Bacteriol*
683 181:6425–6440.
- 684 39. Akashi H, Gojobori T. 2002. Metabolic efficiency and amino acid composition in the
685 proteomes of *Escherichia coli* and *Bacillus subtilis*. *Proc Natl Acad Sci U S A* 99:3695–

- 686 3700.
- 687 40. Weickert MJ, Adhya S. 1993. The galactose regulon of *Escherichia coli*. *Mol Microbiol*
- 688 10:245–251.
- 689 41. Schlegel A, Böhm A, Lee S-J, Peist R, Decker K, Boos W. 2002. Network regulation of the
- 690 *Escherichia coli* maltose system. *J Mol Microbiol Biotechnol* 4:301–307.
- 691 42. Liu P, Danot O, Richet E. 2013. A dual role for the inducer in signalling by MalT, a signal
- 692 transduction ATPase with numerous domains (STAND). *Mol Microbiol* 90:1309–1323.
- 693 43. Danot O. 2010. The inducer maltotriose binds in the central cavity of the tetratricopeptide-
- 694 like sensor domain of MalT, a bacterial STAND transcription factor. *Mol Microbiol* 77:628–
- 695 641.
- 696 44. McCloskey D, Gangoiti JA, Palsson BO, Feist AM. 2015. A pH and solvent optimized
- 697 reverse-phase ion-pairing-LC–MS/MS method that leverages multiple scan-types for
- 698 targeted absolute quantification of intracellular metabolites. *Metabolomics* 11:1338–1350.
- 699 45. Gaudu P, Weiss B. 1996. SoxR, a [2Fe-2S] transcription factor, is active only in its oxidized
- 700 form. *Proceedings of the National Academy of Sciences* 93:10094–10098.
- 701 46. Bradley TM, Hidalgo E, Leautaud V, Ding H, Dimple B. 1997. Cysteine-to-Alanine
- 702 Replacements in the *Escherichia coli* SoxR Protein and the Role of the [2Fe-2S] Centers in
- 703 Transcriptional Activation. *Nucleic Acids Res* 25:1469–1475.
- 704 47. Tseng C-P, Yu C-C, Lin H-H, Chang C-Y, Kuo J-T. 2001. Oxygen- and Growth Rate-
- 705 Dependent Regulation of *Escherichia coli* Fumarase (FumA, FumB, and FumC) Activity. *J*
- 706 *Bacteriol* 183:461–467.
- 707 48. Koo M-S, Lee J-H, Rah S-Y, Yeo W-S, Lee J-W, Lee K-L, Koh Y-S, Kang S-O, Roe J-H.

- 708 2003. A reducing system of the superoxide sensor SoxR in *Escherichia coli*. *EMBO J*
709 22:2614–2622.
- 710 49. Canonaco F, Hess TA, Heri S, Wang T, Szyperski T, Sauer U. 2001. Metabolic flux
711 response to phosphoglucose isomerase knock-out in *Escherichia coli* and impact of
712 overexpression of the soluble transhydrogenase UdhA. *FEMS Microbiol Lett* 204:247–252.
- 713 50. Sauer U, Canonaco F, Heri S, Perrenoud A, Fischer E. 2004. The soluble and membrane-
714 bound transhydrogenases UdhA and PntAB have divergent functions in NADPH
715 metabolism of *Escherichia coli*. *J Biol Chem* 279:6613–6619.
- 716 51. Walsh K, Koshland DE Jr. 1985. Branch point control by the phosphorylation state of
717 isocitrate dehydrogenase. A quantitative examination of fluxes during a regulatory
718 transition. *J Biol Chem* 260:8430–8437.
- 719 52. McKEE JS, Nimmo HG. 1989. Evidence for an arginine residue at the coenzyme-binding
720 site of *Escherichia coli* isocitrate dehydrogenase. *Biochem J* 261:301–304.
- 721 53. LaPorte DC, Walsh K, Koshland DE Jr. 1984. The branch point effect. Ultrasensitivity and
722 subsensitivity to metabolic control. *J Biol Chem* 259:14068–14075.
- 723 54. Zhu G, Golding GB, Dean AM. 2005. The selective cause of an ancient adaptation. *Science*
724 307:1279–1282.
- 725 55. Sun Y, Vanderpool CK. 2013. Physiological consequences of multiple-target regulation by
726 the small RNA SgrS in *Escherichia coli*. *J Bacteriol* 195:4804–4815.
- 727 56. Bobrovskyy M, Vanderpool CK. 2016. Diverse mechanisms of post-transcriptional
728 repression by the small RNA regulator of glucose-phosphate stress. *Mol Microbiol* 99:254–
729 273.

- 730 57. Geanakopoulos M, Adhya S. 1997. Functional characterization of roles of GalR and GalS
731 as regulators of the gal regulon. *J Bacteriol* 179:228–234.
- 732 58. Aki T, Adhya S. 1997. Repressor induced site-specific binding of HU for transcriptional
733 regulation. *EMBO J* 16:3666–3674.
- 734 59. Semsey S, Krishna S, Sneppen K, Adhya S. 2007. Signal integration in the galactose
735 network of *Escherichia coli*. *Mol Microbiol* 65:465–476.
- 736 60. Xu D, Zhang Y. 2013. Ab Initio structure prediction for *Escherichia coli*: towards genome-
737 wide protein structure modeling and fold assignment. *Sci Rep* 3:1895.
- 738 61. Liochev SI, Fridovich I. 2011. Is superoxide able to induce SoxRS? *Free Radic Biol Med*
739 50:1813.
- 740 62. Lo F-C, Lee J-F, Liaw W-F, Hsu I-J, Tsai Y-F, Chan SI, Yu SS-F. 2012. The metal core
741 structures in the recombinant *Escherichia coli* transcriptional factor SoxR. *Chemistry*
742 18:2565–2577.
- 743 63. Kobayashi K. 2017. Sensing Mechanisms in the Redox-Regulated, [2Fe-2S] Cluster-
744 Containing, Bacterial Transcriptional Factor SoxR. *Acc Chem Res* 50:1672–1678.
- 745 64. Ding H, Dimple B. 1996. Glutathione-mediated destabilization in vitro of [2Fe-2S] centers
746 in the SoxR regulatory protein. *Proceedings of the National Academy of Sciences* 93:9449–
747 9453.
- 748 65. Hidalgo E, Dimple B. 1994. An iron-sulfur center essential for transcriptional activation by
749 the redox-sensing SoxR protein. *EMBO J* 13:138–146.
- 750 66. Hidalgo E, Bollinger JM Jr, Bradley TM, Walsh CT, Dimple B. 1995. Binuclear [2Fe-2S]
751 clusters in the *Escherichia coli* SoxR protein and role of the metal centers in transcription. *J*

752 Biol Chem 270:20908–20914.

753 67. Hidalgo E, Dempfle B. 1996. Activation of SoxR-dependent transcription in vitro by

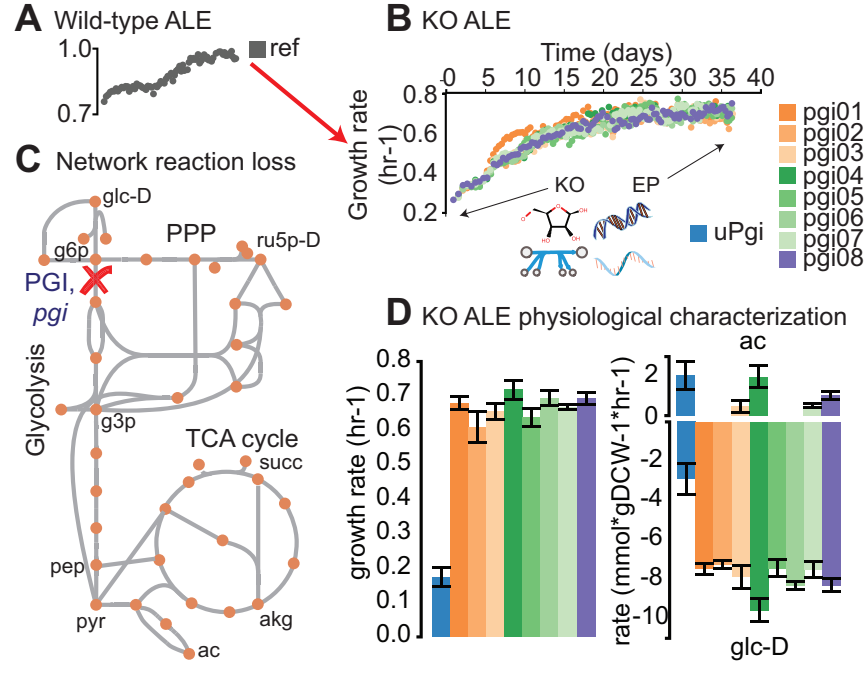
754 noncatalytic or NifS-mediated assembly of [2Fe-2S] clusters into apo-SoxR. J Biol Chem

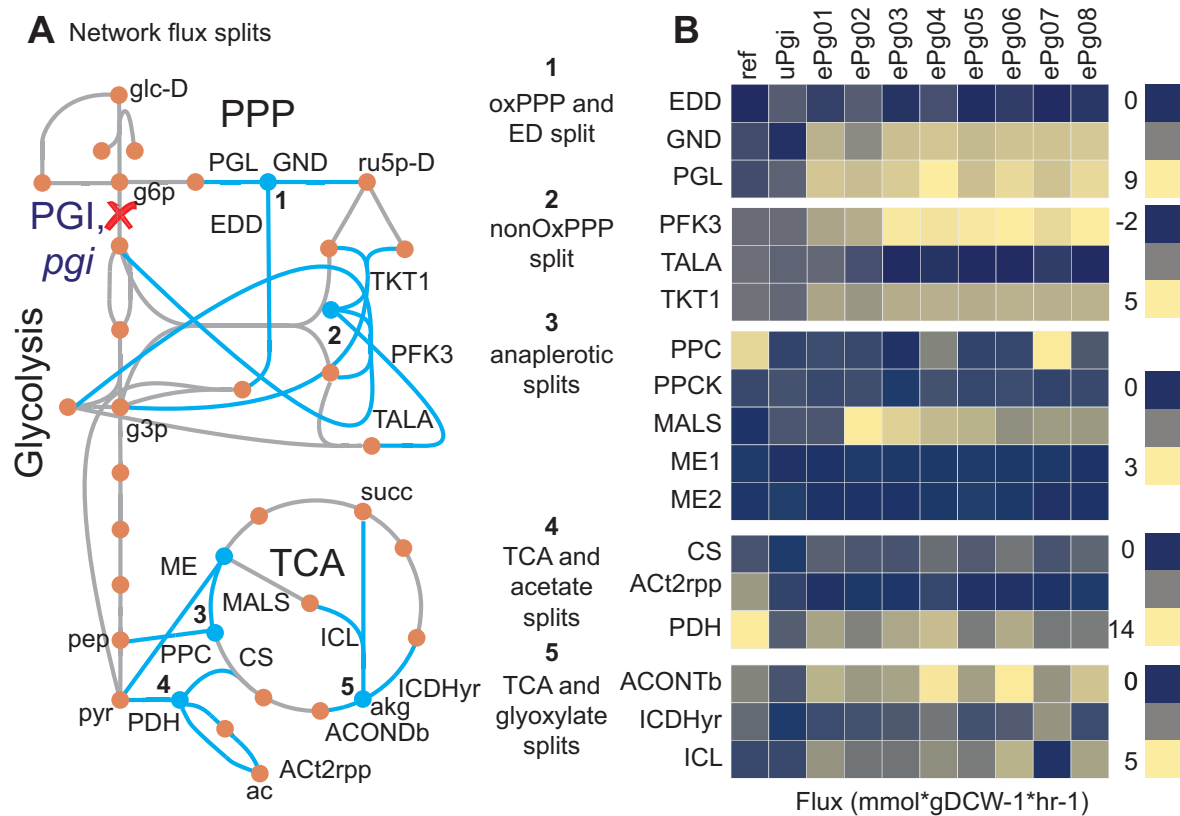
755 271:7269–7272.

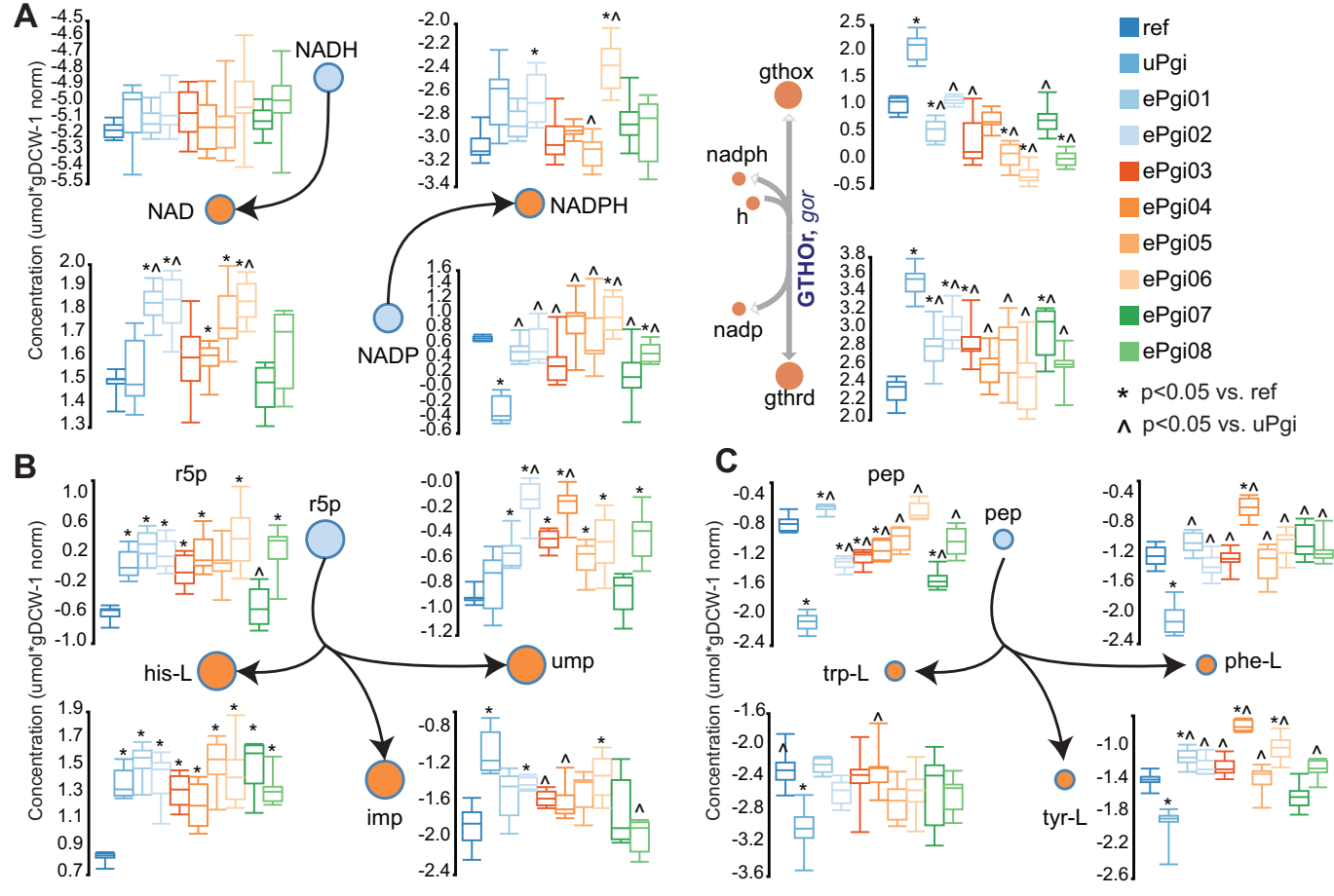
756 68. Watanabe S, Kita A, Kobayashi K, Miki K. 2008. Crystal structure of the [2Fe-2S] oxidative-

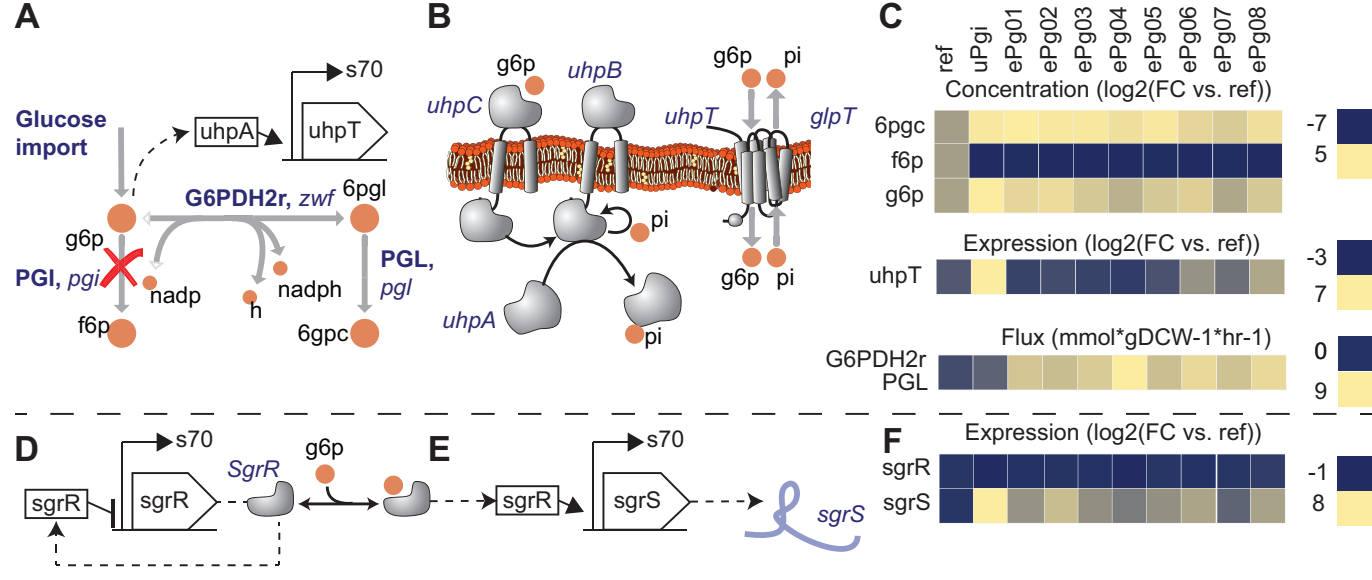
757 stress sensor SoxR bound to DNA. Proc Natl Acad Sci U S A 105:4121–4126.

758



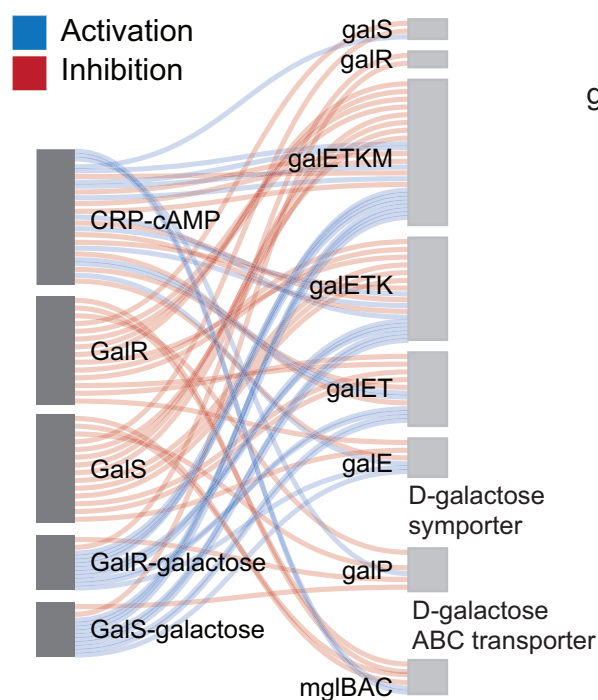




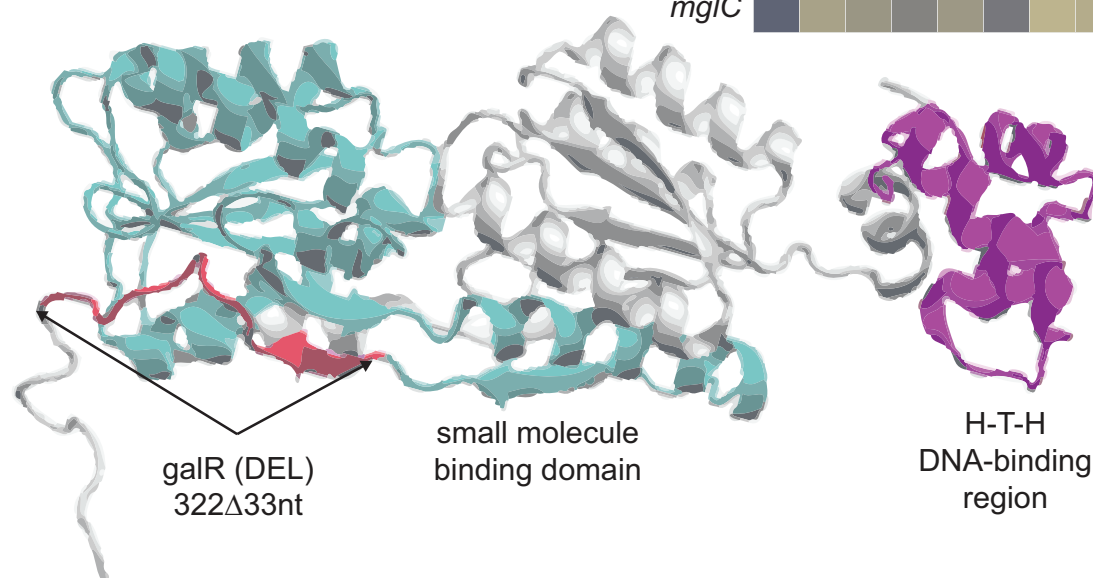


A

Transcription Factor Transcription unit



B



C

